



# ACTIVITY REPORT 2019



## **CORSO DI DOTTORATO DI RICERCA IN FISICA UNIVERSITÀ DEGLI STUDI DI MESSINA**

*Dipartimento di Scienze Matematiche e Informatiche, Scienze  
Fisiche e Scienze della Terra (MIFT)*

**ISSN:  
2038-5889**

**COORDINATORE: VINCENZA CRUPI**

## COORDINATORE DEL DOTTORATO DI RICERCA IN FISICA

Prof.ssa Vincenza Crupi

## COMITATO ORGANIZZATORE

Prof.ssa Vincenza Crupi  
Prof. Lorenzo Torrisi  
Dr. Giuseppe Paladini

## COLLEGIO DOCENTE

### DOCENTI E RICERCATORI UNIME

<b>Prof.ssa Branca Caterina</b>	<b>Prof. Mandaglio Giuseppe</b>	Prof. Sergi Alessandro
Dr. Corsaro Carmelo	<b>Prof. Neri Fortunato</b>	<b>Prof. Torrisi Lorenzo</b>
Dr. Costa Dino	<b>Prof.ssa Orecchio Barbara</b>	<b>Prof. Trifirò Antonio</b>
<b>Prof.ssa Crupi Vincenza</b>	<b>Prof. Patanè Salvatore</b>	Prof.ssa Trimarchi Marina
<b>Prof.ssa D'Angelo Giovanna</b>	Prof.ssa Presti Debora	<b>Prof.ssa Venuti Valentina</b>
<b>Prof.ssa Fazio Enza</b>	<b>Prof. Prestipino Giarritta Santi</b>	Prof. Wanderlingh Ulderico
<b>Prof. Magazù Salvatore</b>	<b>Prof.ssa Saija Rosalba</b>	
<b>Prof. Majolino Domenico</b>	<b>Prof. Savasta Salvatore</b>	

### PERSONALE NON ACCADEMICO DIPENDENTE DI ALTRI ENTI E PERSONALE DOCENTE DI UNIVERSITÀ STRANIERE

Dr.ssa Cutroneo Mariapompea  
Dr. Gucciardi Pietro Giuseppe  
Dr. Maragò Onofrio  
Dr. Micali Norberto  
Dr.ssa Puglisi Rosaria Anna  
Dr. Saija Franz  
Dr. Trusso Sebastiano

I membri del collegio evidenziati in **grassetto** fanno parte del consiglio ristretto di dottorato.



**DOTTORATO DI RICERCA IN FISICA  
UNIVERSITÀ DEGLI STUDI DI MESSINA**

**ACTIVITY REPORT  
2019**

**ISSN 2038-5889**

**DIPARTIMENTO DI SCIENZE MATEMATICHE E  
INFORMATICHE, SCIENZE FISICHE  
E SCIENZE DELLA TERRA**

Università degli Studi di Messina  
Viale F. Stagno d'Alcontres 31, 98166, Messina

**VINCENZA CRUPI COORDINATORE**

<https://www.unime.it/it/dottorato/fisica>

# Indice

## Prefazione

### Reports Studenti di Dottorato Ciclo XXXIII

C. CALABRETTA, M. AGATI, M. ZIMBONE, S. BONINELLI, A. CASTIELLO, A. PECORA, G. FORTUNATO, L. CALCAGNO, L. TORRISI, F. LA VIA: <i>Laser annealing process of P and Al implanted 4H-SiC epitaxial layers</i> . . . . .	6
S. LONGO, S. CAPUANI, E. FAZIO: <i>Clinical scanners for wooden Cultural Heritage investigations: X-Ray Multislice Computed Tomography (MSCT) and Magnetic Resonance Imaging (MRI)</i> . . . . .	11
F. PATTI, R. SAIJA, M.A. IATÌ, O. M. MARAGÒ: <i>Active Cooling with Optically Levitated Nanoparticles</i> . . . . .	15
A. SETTINERI, O. DI STEFANO, S. SAVASTA: <i>Interaction of Mechanical Oscillators by means of the quantum vacuum</i> . . . . .	17

### Reports Studenti di Dottorato Ciclo XXXIV

G. BORGH, C. BONGIORNO, E. FAZIO, A. LA MAGNA, G. MANNINO, F. NERI, S. SCALESE, R.A. PUGLISI: <i>Advanced processing for Silicon Nano-Wire based Solar Cells</i> . . . . .	21
S. GURGONE, V. VENUTI, D. BORZELLI, P. DE PASQUALE, M. MEZZETTI, D. BERGER, G. ACRÌ, A. D'AVELLA: <i>Effect of Extended Practice on Adaptation to Virtual Surgeries</i> . . . . .	25
B. MAZZA, S. PATANÈ, F. CORDIANO, M. GILIBERTO, G. FRANCO: <i>Electrical Overstress effect characterization on PowerMOS Trenchfet and correlation with Time dependent dielectric breakdown</i> . . . . .	29
D. PISTONE, G. MANDAGLIO: <i>Multiplicity dependence of <math>K^*(892)^\pm</math> resonance production in proton-proton collisions at <math>\sqrt{s} = 13</math> TeV</i> . . . . .	33
P. POLIMENO, A. VELTRI, G. VOLPE, M. A. IATÌ, O. M. MARAGÒ, R. SAIJA: <i>Modeling of resonant gain metal/dielectric nanoshell in optical tweezers</i> . . . . .	37
D. ROMANO, S. MAGAZÙ, F. ITALIANO, G. SABATINO, A. TRIPODO, M. T. CACCAMO: <i>A brief overview on Radon emanation from natural solid materials</i> . . . . .	41

### Reports Studenti di Dottorato Ciclo XXXV

L. ANOLDO, S. PATANÈ, S. BEVILACQUA, A. RUSSO: <i>Novel idea around Wafer Level Burn-In</i> . . . . .	45
L. BIONDO, G. MANDAGLIO ON BEHALF OF EEE COLLABORATION: <i>Angular and Spatial Resolution of EEE Telescopes</i> . . . . .	50
G. GALLO, V. ROMANO, G. D'ANGELO:	

<i>Production and Raman characterization of 2D materials for energy applications</i> . . . . .	54
R. MUSOTTO, M. DE PITTÀ, G. PIOGGIA: <i>Principles of a neuron-glia tripartite synapse based biomorphic processing unit</i> . . . . .	58
A. ROSANO, A. FERRETTI, A. BIANCHI: <i>Eco-friendly Gas Mixtures for the Resistive Plate Chambers of the ALICE Muon Spectrometer</i> . . . . .	61
A. SAIDI: <i>Effect of temperature on the absorption spectrum of Lithium deposited on argon cluster</i> . . . . .	66
<b>Seminari del Dottorato di Ricerca in Fisica</b>	
Elenco dei Seminari Obbligatori . . . . .	72
Premi e Riconoscimenti . . . . .	82
<b>Organizzazione del Dottorato di Ricerca in Fisica</b>	
Organizzazione . . . . .	84
Piano didattico del Dottorato di Ricerca in Fisica . . . . .	85
<b>Collegio dei Docenti del Dottorato di Ricerca in Fisica</b>	
Collegio Docente . . . . .	93
<b>Tesi e Argomenti di Ricerca Studenti del Dottorato di Ricerca in Fisica</b>	
Tesi degli Studenti del Ph.D. in Fisica (Ciclo XXXII) . . . . .	96
Argomento di Ricerca degli Studenti del Ph.D. in Fisica (Cicli XXXIII & XXXIV) . . . . .	97
<b>Pubblicazioni degli Studenti del Dottorato di Ricerca in Fisica</b>	
Pubblicazioni degli Studenti del Dottorato in Fisica (XXXIII Ciclo) . . . . .	99
Pubblicazioni degli Studenti del Dottorato in Fisica (XXXIV Ciclo) . . . . .	101
<b>Galleria Fotografica degli Studenti del Dottorato di Ricerca in Fisica</b>	
Studenti del Dottorato di Ricerca in Fisica del XXXIII Ciclo . . . . .	104
Studenti del Dottorato di Ricerca in Fisica del XXXIV Ciclo . . . . .	105
Studenti del Dottorato di Ricerca in Fisica del XXXV Ciclo . . . . .	106
<b>Alta Formazione, Ricerca Scientifica e Relazioni Internazionali</b>	
Alta Formazione, Ricerca Scientifica e Relazioni Internazionali . . . . .	108

Messina, 1 Ottobre 2019

Carissimi Tutti,

Collegli del Collegio dei Docenti e Studenti di Dottorato,

È con grandissimo piacere che come ogni anno il Corso di Dottorato di Ricerca in Fisica, incardinato presso il Dipartimento MIFT - Università degli Studi di Messina, apre il nuovo anno accademico con un appuntamento graditissimo, ovvero la stesura dell'*Activity Report*. Quest'anno siamo arrivati alla X edizione con *l'Activity report 2019*, che come è consuetudine raccoglie testimonianza puntuale e dettagliata dell'attività formativa e di ricerca di tutti gli studenti di Dottorato dei Cicli ancora attivi per l'anno accademico in corso.

È per me particolare privilegio quest'anno, in qualità di nuovo Coordinatore, continuare questa tradizione iniziata nel 2010 in occasione della **I Giornata di Studio del Dottorato di Ricerca in Fisica** (10 Novembre 2010), organizzata dal collega **Prof. Lorenzo Torrisi**, già coordinatore del Dottorato di Ricerca in Fisica a partire dall'anno accademico 2008/2009, fino all'anno accademico 2018/2019.

Desidero ringraziare di cuore a nome dei collegli e degli studenti di dottorato dei cicli passati ormai conclusi e dei cicli ancora attivi, l'amico e collega Lorenzo per questi **dieci anni di successi e di traguardi** raggiunti dal nostro dottorato, grazie al suo infaticabile e costante impegno. Impegno tradotto in termini di **sinergiche collaborazioni scientifiche** tra i nostri discenti e i ricercatori delle più prestigiose Università e Centri di Ricerca italiani e stranieri e, impegno in termini di **internazionalizzazione**, grazie all'opportunità offerta ai nostri dottorandi di trascorre periodi, anche prolungati, di ricerca all'estero, nonché all'accoglienza di studenti stranieri. Successi testimoniati dalle numerose pubblicazioni scientifiche su prestigiose riviste internazionali che hanno visto e vedono i nostri dottorandi tra i principali co-autori e traguardi raggiunti grazie all'intuito, alla convinzione e alla dedizione incondizionata che Lorenzo ha saputo riservare al Nostro Dottorato in tutti questi anni.

Ritengo che un buon Corso di Dottorato di Ricerca debba essere sempre attento e sensibile alle necessità dei propri studenti, erogando loro un'offerta formativa quanto più completa possibile ed una sempre più variegata attività di ricerca in linea con le tematiche scientifiche più attuali. Particolare attenzione va inoltre posta nei confronti degli "eventuali" discenti stranieri, partendo da una semplificazione delle modalità di partecipazione all'esame di ammissione al corso di dottorato, in linea con le esigenze di **internazionalizzazione dell'Ateneo di Messina** nonché con il **Corso di Studi Magistrale in Fisica indirizzo Condensed Matter Physics** (Classe LM-17, Fisica), quest'ultimo totalmente erogato in lingua Inglese, incardinato presso il Dipartimento MIFT. Vale la pena ricordare che il Nostro Dottorato di Ricerca in Fisica in passato è stato pioniere in tal senso, con i vari studenti stranieri in co-tutela di tesi di dottorato a seguito di accordi con Università Straniere di prestigio. Attualmente tra gli studenti del I anno del XXXV Ciclo, appena partito, il Corso di Dottorato annovera una studentessa di cittadinanza Tunisina.

Il Dottorato di Ricerca in Fisica dell'Università degli Studi di Messina intende raccogliere e vincere questa ed altre "sfide". Auguro pertanto a tutti, ai componenti del Collegio dei Docenti, ai discenti tutti, a partire dal ciclo XXXIII, che si appresta a concludere il suo percorso di massima formazione universitaria, passando dal ciclo XXXIV che si trova a "metà" del suo percorso di studio e di ricerca fino al ciclo XXXV, al quale dedico un pensiero ancora più affettuoso se ciò mi è concesso, perché è con esso che ha inizio questa mia avventura, impegnativa ma al tempo stesso molto formativa, ne sono certa, in veste di Coordinatore e, a me stessa... di riuscire a superare tutte quelle sfide scientifiche che il mondo dell'alta formazione universitaria e della ricerca ci vorrà porre e proporre, lavorando tutti insieme (docenti e discenti) in grande sinergia.

Buon lavoro a TUTTI!

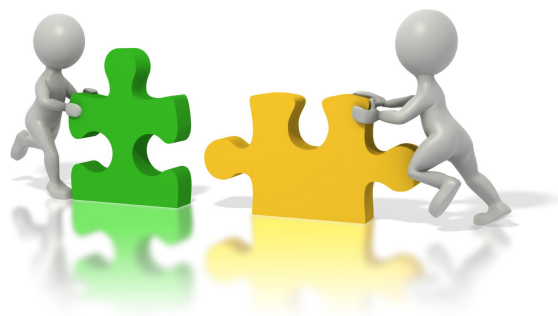
# PREFAZIONE

## PREFAZIONE

---

Il Dottorato di Ricerca è un percorso di alta formazione tecnico-scientifica che garantisce strumenti metodologici e competenze tali da delineare una professionalità altamente qualificata nell'ambito della ricerca e dell'innovazione tecnologica. Il dottorato di ricerca mira a trasferire ai dottorandi una cultura scientifica avanzata, le competenze e gli strumenti metodologici necessari per esercitare attività di ricerca di alta qualificazione. Il Dottore di Ricerca è un "problem solver" con alta qualificazione scientifica che può ricoprire profili professionali di elevato livello grazie alla capacità di affrontare in modo autonomo i problemi ed alla predisposizione a lavorare in team, spesso in contesti di carattere internazionale. Il Dottore di Ricerca è inoltre in grado di supportare processi di trasferimento tecnologico e di contribuire a sviluppare una vera e propria cultura dell'innovazione nel contesto in cui opera. Nel suo iter formativo, il Dottore di Ricerca si arricchisce nel dialogo con la comunità scientifica internazionale sulle tematiche più attuali della Ricerca & Sviluppo (R&S), maturando familiarità verso le nuove tecnologie e la loro ricaduta sul sistema produttivo, delineandosi come una figura strategica capace di coniugare sinergicamente Università ed Impresa. Il Dottore di Ricerca è un manager della ricerca che possiede esperienza nella ricerca universitaria e conoscenza delle esigenze industriali e dei processi di trasferimento dei risultati della ricerca, contribuendo ad aumentare il livello di innovazione industriale. La capacità di gestire l'innovazione e l'originalità creativa nell'elaborazione e nella realizzazione di progetti e servizi acquisite dal Dottore di Ricerca sono aspetti strategici che possono risultare particolarmente utili all'interno delle Piccole e Medie Imprese (PMI) che intendano investire in R&D. Le proiezioni della VII Indagine nazionale dell'Associazione dottorandi e dottori di ricerca (ADI) su Dottorato e Post-Doc mostrano che - con i numeri attuali del reclutamento universitario - più del 90% dei ricercatori nella fase iniziale della loro carriera abbandonerà l'Università dopo un percorso fatto di contratti precari che può durare

fino a 12 anni. Il sotto-finanziamento strutturale dell'Università e il mancato ricambio generazionale nel personale di ruolo rappresentano la prima, cronica, emergenza che mette a rischio la sopravvivenza dell'intero sistema della formazione e della ricerca: è necessario dunque dare priorità ad un piano di rifinanziamento e reclutamento in grado di riportare il personale docente almeno ai livelli del 2008. Rimane sul tavolo una domanda di fondo: in che modo i settori pubblico e privato del nostro Paese sono in grado di mettere a frutto le competenze accumulate dai dottori di ricerca? Dalle informazioni oggi disponibili emerge dunque un quadro poco confortante: la grande maggioranza dei dottori di ricerca è occupata con contratti precari; il settore privato assorbe meno del 40% dei dottori di ricerca e, al suo interno, l'industria ne impiega solo un quarto. I dottori di ricerca vengono scarsamente valorizzati, con il loro bagaglio di competenze e conoscenze nel sistema produttivo e imprenditoriale, come una risorsa strategica per l'innovazione e lo sviluppo del tessuto socio-economico nazionale. Da qui le manifestazioni di interesse, se pur limitate, da parte delle Imprese e le azioni intraprese dalle Università; infatti, ricerca e sviluppo sono i due obiettivi su cui il mondo delle imprese e quello della formazione hanno la possibilità di fare fronte comune.



Il dottorato industriale, come si legge nella definizione del Decreto Ministeriale dell'8 febbraio 2013 numero 45 all'articolo 11, può essere un mo-

tore di crescita e sperimentazione sia per le aziende che per le università. Il Dottorato Industriale è un percorso triennale che prevede un progetto di ricerca mirato alla formazione di un dottorando con competenze di tipo applicativo. L'iniziativa è portata avanti grazie alla collaborazione tra l'università, un'azienda e centri di ricerca, anche internazionali. Lo studente dottorando svolge le proprie attività lavorative sia presso l'azienda che presso gli enti di ricerca, dedicando il proprio tempo lavorativo al progetto di dottorato industriale, i cui risultati saranno effettivamente applicati anche in un contesto aziendale. Dal canto suo, l'azienda ha a propria disposizione un candidato in grado di portare avanti un progetto di ricerca di alta qualità, i cui risultati possono condurre ad esiti positivi in termini di implementazione industriale, con impatto immediato. Allo stesso tempo, l'azienda ha la possibilità di rafforzare le proprie relazioni con dei partner universitari, ponendo le basi per nuove prospettive di ricerca e di collaborazione fra Ateneo e settore privato. Pertanto, il dottorando può acquisire preliminari competenze per divenire in futuro un esperto di innovazione tecnologica, potendo così accedere a posizioni manageriali negli ambiti industriali. Tutto ciò anche per favorire l'inserimento dei Dottori di Ricerca nel mondo economico-produttivo del nostro Paese senza limitare gli sbocchi professionali al solo mondo accademico. Ciò è fondamentale in un momento in cui l'Italia ha bisogno di ritrovare competitività. In questo contesto, il Dottore di Ricerca può assumere il ruolo di Innovation Manager, per inserirsi nelle imprese e nelle Pubbliche Amministrazioni come "anello di congiunzione" tra il sistema della ricerca pubblica (che peraltro ha bisogno di accedere a capitali privati) e quello produttivo. Nell'ambito del "Programma Operativo Nazionale Ricerca e Innovazione 2014-2020: Dottorati innovativi con caratterizzazione industriale", nel 2018 è stata presentata una proposta di progetto di Dottorato Industriale da parte dei Professori del Dipartimento di Scienze Matematiche e Informatiche, Scienze Fisiche e Scienze della Terra (MIFT) dell'Università degli Studi di Messina (Prof. Enza Fazio, Prof. Fortunato Neri), del Consiglio Nazionale delle Ricerche –

Messina, Italy  
December, 2019

Istituto per la Microelettronica e Microsistemi (CNR-IMM) di Catania (Dr.ssa Rosaria Anna Puglisi, Dr. Guglielmo Fortunato), dell'impresa "Elettronica Tirrito s.r.l.", in collaborazione con l'Università di Catania e l'Università di Paderborn che ha come tema lo sviluppo di un metodo di drogaggio di semiconduttori tramite molecole organiche autoassemblate (MD) con possibili applicazioni anche nel campo delle celle solari di terza generazione. La proposta si inserisce perfettamente all'interno dell'area tematica "Industria intelligente e sostenibile, energia e ambiente".



Oggi, il progetto approvato e finanziato è stato incardinato al XXXV ciclo del Corso di Dottorato di Ricerca in Fisica presso l'Università degli Studi di Messina. Si tratta del primo caso di progetto di "Dottorato di Ricerca Industriale" di area Fisica finanziato le cui azioni per lo sviluppo delle attività del progetto sono oggi in essere. L'auspicio è che altri progetti a caratteri industriale vengano proposti nei prossimi anni, rappresentando un valore aggiunto per il Dottorato di Ricerca in Fisica, per il Dipartimento MIFT dell'Università degli Studi di Messina e per l'intero Ateneo messinese.

**E. Fazio, F. Neri, V. Crupi**  
Dipartimento MIFT,

Università degli Studi di Messina,  
Viale F. Stagno d'Alcontres, 31, 98166 Messina, Italy.

**R. A. Puglisi**  
CNR-IMM,

Strada Ottava 5, Zona Industriale, 95121 Catania, Italy.

REPORTS  
STUDENTI DI DOTTORATO DI  
RICERCA  
CICLO XXXIII

# Laser annealing process of P and Al implanted 4H-SiC epitaxial layers

C. Calabretta<sup>1-2,\*</sup>, M. Agati<sup>2</sup>, M. Zimbone<sup>2</sup>, S. Boninelli<sup>2</sup>, A. Castiello<sup>3</sup>, A. Pecora<sup>3</sup>, G. Fortunato<sup>2</sup>, L. Calcagno<sup>4</sup>, L. Torrisi<sup>1</sup>, F. La Via<sup>2</sup>

<sup>1</sup>MIFT, Università degli studi di Messina, Viale F. Stagno d'Alcontres, 31-98166 Messina, Italy

<sup>2</sup>CNR-IMM, VIII Strada, 5, 95121 Catania, Italy

<sup>3</sup>CNR-IMM, Via del Fosso del Cavaliere, 100-00133 Roma

<sup>4</sup>DFA Dipartimento di Fisica e Astronomia, Università degli studi di Catania, Via S. Sofia 64, 95123 Catania, Italy;

\*Corresponding Author email: [cristiano.calabretta@unime.it](mailto:cristiano.calabretta@unime.it)

## Abstract

This work describes the development of a new method for ion implantation induced crystal damage recovery using multiple XeCl (308 nm) laser pulses with a duration of 30 ns. Experimental activity was carried on single phosphorus (P) as well as double phosphorus and aluminum (Al) implanted 4H-SiC epitaxial layers. The activity outcome shows that laser annealing allows to achieve full crystal recovery in the energy density range between 0.50 and 0.60  $J/cm^2$ . Moreover, laser treated crystal shows an almost stress-free lattice with respect to thermally annealed samples that are characterized by high point and extended defects concentration. Laser annealing process allows to strongly reduce carbon vacancy ( $V_C$ ) concentration in the implanted area and to avoid intra-bandgap carrier recombination centres. Implanted area was almost preserved, except for some surface oxidation processes due to oxygen leakage inside the testing chamber. However, the results of this experimental activity give way to laser annealing process viability for damage recovery and dopant activation inside the implanted area.

**Keywords:** 4H-SiC, laser annealing, ion implantation, dopant activation, micro-Raman, TEM.

## Introduction

4H-SiC popularity, due to its favourable properties for high-temperature and high-power applications, has recently grown leading to its expansion in semiconductor devices, and particularly in MOSFET technology. The realization of MOSFET selected doped areas, such as the source and body regions, are achieved through ion implantation. However, low diffusivity of mostly used dopants in SiC requires the use of multi-ion implantation with different energies and doses to achieve selected uniformly doped area. The realization of MOSFET's n-type source region occurs through phosphorus ion implantation, while the p-type body region is obtained using Al. The use of these processes involves the generation of a considerable implantation defectiveness, which is only partially recovered by conventional thermal treatments. Moreover dopant activation is strongly limited both by dopant solid solubility, and by the attainable annealing temperature in conventional high temperature (HT) steps. Thermal annealing is also involved in  $V_C$  generation under standard thermal equilibrium processes so that new non equilibrium methods based on short time annealing duration are required. A comprehensive description of thermal annealing dynamics is provided by transient model activation [1], which states that the ini-

tial activation speed for both donor and acceptor impurities is extremely high and decrease rapidly with time. Indeed, rapid thermal annealing systems, are able to obtain high dopant incorporation eluding the usual impurity deactivation due to solid solubility lowering during cooling ramps. In particular, laser annealing technique counts on ramps as high as  $10^9$  K/s and allows to obtain much higher temperatures than conventional processes. After first Hishida [2] and Ahmed's [3] laser annealing attempts on 4H-SiC, Tanaka [4] pointed out that 4H-SiC melt phase annealing was not a suitable post implant treatment due to the impossibility of obtaining full 4H-SiC epitaxial regrowth. Consequently excimer laser pulses under sub-melting condition were proposed to perform a sequence of rapid thermal annealings in the ns time regime. Boutopoulos [5] confirmed the viability of this method carrying out a structural micro-Raman analysis of multi-shot laser annealing on Al implanted 4H-SiC. He observed how Nd:Yag (355 nm) multiple irradiation method was able to significantly recover reflectivity signal intensity in the Reststrahlen band. However, TEM analysis showed the formation of polycrystalline structure after laser annealing process. Similar results are stated by Mazzamuto [6], who claims to obtain full epitaxial regrowth from SiC melting phase, though TEM analysis show polycrystalline lattice recovery after ion implantation. The aim of this work

is to offer a pioneering characterization of laser annealing effects on implanted SiC with particular concern to phase separation energy thresholds related to SiC non-congruent melting. We perform an effective study of the exploitable XeCl laser energies, as well as an atomic scale characterization that confirms the complete 4H polytype maintenance under sub-melting regime.

## Material and Methods

Experimental activity was conducted on SiC wafer supplied by Cree with a nitrogen concentration of  $10^{18}$  N/cm<sup>3</sup>. A 6 μm epitaxial layer was then grown along the (0001) 4° off-axis direction through low pressure hot wall chemical vapor deposition. Source P ion implantation was performed at 500 °C with energies between 30 and 200 keV and fluences ranging from  $10^{13}$  to  $10^{14}$  cm<sup>-2</sup> in order to obtain an almost uniform doped layer, 200 nm thick, with a concentration of  $10^{20}$  P/cm<sup>3</sup>. In the double implanted sample a further multistep implantation was performed with Al doses between  $10^{12}$  and  $10^{13}$  cm<sup>-2</sup> at 400 °C. The wafer was then cut into several squares using a diamond tip to obtain different samples on which we performed the tests. In order to eliminate any impurities on the surface, the samples were subsequently bathed in isopropyl alcohol and dried by compressed air jet. Laser treatments were carried out through a LPX 300 XeCl pulsed excimer laser (308 nm), Lambda Physics, Göttingen, Germany) with 40 Hz repetition rate. The samples were so irradiated by a 1 mm x 20 mm uniform intensity profile radiation inside a chamber under helium atmosphere at a pressure of  $1 \times 10^{-2}$  mbar. Substrate holder inside the chamber was heated at a temperature of 580 °C and a mobile stage allowed to implement an irradiation process until 1000 shots/point. On the other hand, isochronical (1 h) thermal annealings were carried out at 1650 °C, 1700 °C, 1750 °C for P implanted samples, while a sample subjected to double implantation was annealed at 1650 °C for 30 min. The effectiveness of laser treatments was verified by micro-Raman and photoluminescence analysis, carried out with a He-Cd laser source (325 nm) and a LabRAM HR spectrofluorimeter (Horiba Jovin Yvon, Kyoto, Japan) with a 1800 l/mm grating. Structural investigation was performed using TEM microscopy on a 2010F Jeol microscope (Tokyo, Japan) equipped with a Gatan image filter for electron energy loss spectroscopy (EELS).

## Results and discussion

Laser thermal processing was first inspected by Raman spectroscopy. This technique is widely used for SiC characterization since it is non-destructive, requires no special sample preparation and presents high sensitivity on structural changes, so that a survey methodology to verify crystal damage recovery can be obtained. Indeed, it is known that ion implantation process generates damage inside the crystal, and although implantation is carried out at 550 °C to avoid lattice amorphization, a decrease of first order Raman peaks intensities has been observed

proportional to implantation dose [6]. With the increase in the number of laser shots it is possible to observe the recovery of the 4H-SiC characteristic phonon modes: E<sub>2</sub>(TA) at 205.5 cm<sup>-1</sup>, A<sub>1</sub>(LA) at 612.1 cm<sup>-1</sup>, E<sub>2</sub>(TO) at 776.0 cm<sup>-1</sup>, E<sub>1</sub>(TO) at 798.6 cm<sup>-1</sup> and A<sub>1</sub>(LO) at 967.3 cm<sup>-1</sup>. The increase in the intensity of these Raman peaks as a function of the radiation energy density shows how the laser is able to produce an annealing effect to recover sample crystallinity. Transverse optic E<sub>2</sub>(TO) mode signal intensities were extrapolated from Raman spectra and are reported in Figure 1a. In the case of 1 shot/point, crystal recovery is weak compared to as implanted sample signal. However, when the number of shots is increased up to 1000 shots/point, it can be seen that both samples with single and double implant exhibit E<sub>2</sub>(TO) signal intensity enhancement and existence of 3 regions is found. Up to 0.30 J/cm<sup>2</sup> E<sub>2</sub>(TO) peak intensity remains low. Between 0.30 J/cm<sup>2</sup> and 0.60 J/cm<sup>2</sup> the TO mode signal sharply rises up to its maximum, until the onset of phase separation, where 4H-SiC Raman signal E<sub>2</sub>(TO) goes down and crystalline silicon peak at 520 cm<sup>-1</sup> together with low carbon G band at 1592 cm<sup>-1</sup> are detected. In thermally annealed samples, the attempt to increase the fraction of dopant activated by increasing the annealing temperature from 1650 °C to 1750 °C produces a 15% reduction in E<sub>2</sub>(TO) signal intensity and broadening from 5.3 to 8.1 cm<sup>-1</sup>, due to the increase in thermal generated defectiveness not only within the projected range of the system but throughout the entire sample, so that worsening of crystallinity is therefore deducible. Raman signals coming from samples subjected to double implantation are slightly lower than the single implantation one. In this case, in fact, the presence of a second 700 nm deep layer involves an increase of damage and consequently a lowering of the Raman peak intensities. When the sample is irradiated with an energy above the 0.60 J/cm<sup>2</sup> threshold, Raman spectrum shows a further peak at 520 cm<sup>-1</sup>. This new vibrational frequency is associated with crystalline Si layers deposited on surface due to phase separation occurring when SiC melting temperature is reached. The identification of this energy threshold is consistent with the results coming from numerical solution of heat flow equation and expressed as

$$\frac{\partial T}{\partial x} = \frac{\alpha}{\rho C_p} I(z, t) + \frac{1}{\rho C_p} \frac{\partial}{\partial z} \left( k \frac{\partial T}{\partial x} \right) \quad (1)$$

$$I(z, t) = I_0(t) (1 - R) e^{-\alpha z} \quad (2)$$

where T represents the absolute temperature, ρ sample density, C<sub>p</sub> the specific heat, k is thermal conductivity, I<sub>0</sub> is laser intensity at the surface, R is surface reflectivity, α the optical absorption, z the depth from surface, I(z, t) laser intensity. According to Equations (1) and (2), the melting threshold of as-implanted SiC irradiated with 30 ns XeCl pulse length stands over 0.60 J/cm<sup>2</sup> [7], while to induce phase separation in crystalline SiC a laser energy equal to 1 J/cm<sup>2</sup> is required.

This prediction is based on the assumption that, when the implanted layer thickness exceeds 200 nm, optical parameters are in reasonable agreement with that of bulk amorphous SiC. Samples subjected to thermal annealing also

show a deviation from the nominal 4H-SiC vibrational frequency between 1650 °C and 1750 °C (*Figure 1b*). The effect arising from such a high thermal budget results in the generation of a compressive (P implanted) and tensile (P and Al implanted) stress particularly assessable along the planar component, since the E2(TO) modes have an atomic displacement perpendicular to the c axis [8].

$$\Delta\omega_{E_2} = (2a_{E_2} + b_{E_2})P = 3.59P \quad (3)$$

$$a_{E_2} = -1.55\text{cm}^{-1}/\text{GPa} \quad (4)$$

$$b_{E_2} = -0.74\text{cm}^{-1}/\text{GPa} \quad (5)$$

where  $\Delta\omega_{E_2}$  is the phonon frequency shift,  $a_{E_2}$  and  $b_{E_2}$  are the phonon deformation and P is the in plane pression, it is therefore possible to provide an estimate of the stress, which in the case of thermally annealed samples ranges from 130 to 172 Mpa increasing with temperature. The usual thermal processes generate a strong stress contribution that is due to multiple factors. In small part this is due to the incorporation of the P or Al dopant responsible for opposing stress contributions and to the shear stress between the implanted area and the underlying epitaxial layer, while the predominant role is related to the creation of a high concentration of both point and extended defects in the implanted region [9]. Samples subjected to laser annealing show much smaller stress values. Especially in high recovery ranges between 0.50 and 0.60 J/cm<sup>2</sup>, vibrational frequencies close to epitaxial mode were detected and calculated stress does not exceed 50 MPa, so that almost stress-free samples resulted from laser annealing process. The presence of an important crystal recovery effect is also visible by mean of the photoluminescence analysis revealing 4H-SiC band-gap signal recovery at 390 nm through 1000 shots/point irradiation. Bandgap emission signal tends to reach the intensity of thermally annealed samples in the energy range between 0.50 and 0.60 J/cm<sup>2</sup>. Moreover furnace-treated samples show a large spectral defect related emission region peaked at 490 nm and with 175 nm FWHM which corresponds to wide defectiveness area within the implant region. Out-of-equilibrium annealing regimes, on the other hand, restore a spectrum with lower intra-bandgap peak by a factor of 8-9, as well as shifted to 550 nm emission wavelength similar to those of epitaxial layer (as reported in[10]). Bright field TEM analyses were performed to structurally characterize the effects due to laser irradiation. Several extended defects are detected inside the implanted area, as shown in *Figure 2a* in the case of the 0.60 J/cm<sup>2</sup> laser annealed source implant sample. The presence of these defects allows to quantify the portion of implant survived to laser interaction. It was possible to estimate that within the 0.40 J/cm<sup>2</sup> irradiated sample an implanted area of almost 130 nm was preserved (image not shown), while with the increase of laser energy density this fraction is thinned to 90 nm . However, the cross section confirms the data obtained with Raman spectroscopy. In fact, in the inset of *Figure 2a*, the diffraction pattern acquired on the [10-1 0] zone axis shows the full crystallinity of the implanted area. From *Figure 2a* we can see that laser interaction

gives rise to a certain degree of surface misalignment, although the crystal is kept under the 4H polytype. *Figure (2b)* shows the 0.40 J/cm<sup>2</sup> irradiated sample HRTEM. It can be highlighted that inspected region maintained the ABAC stacking characteristic of the 4H polytype under the [11-20] zone axis up to the top. It is evident that the crystal did not undergo any melting process that would have produced 3C-SiC layer on surface combined with the SiC columnar regrowth from the melt/solid interface [6]. However, since SiC (0001) is characterized by a relatively important surface energy [11], high temperature treatments commonly promote surface desorption of silicon atoms from the surface and consequent micro-step formation. Nevertheless, the presence of a further contribution to surface misalignment on many samples is present in the form of spherical aggregates with average size of 131 nm and with 21 % of surface coverage. To perform an elemental analysis the sample was analyzed using STEM-EELS spectrum imaging. In *Figure 3b* we reported the EELS spectra acquired in correspondence of the region 1 and 2 of the sample, as indicated in *Figure 3a*. In the EELS spectrum corresponding to region 1, we can easily recognize the characteristic SiO<sub>2</sub> spectrum, where it is possible to identify the Si-L<sub>1</sub>, Si-L<sub>2,3</sub> and O-K edges. The EELS spectrum corresponding to region 2, instead, shows the typical SiC signal coming from bulk SiC. Therefore, once identified surface aggregates as SiO<sub>2</sub> compounds, it is possible to attribute their formation to the presence of residual O in the chamber as an etching source. Studies of the reaction between O and SiC [12] allow, in fact, to state that the interaction between O and SiC at high temperatures is not only present in the form of passive oxidation, but at low pressures it results in phenomena of active oxidation, leading to surface etching and contextual important role in C surface segregation. It can therefore be inferred that O presence in chamber may have played a role in superficial roughness while etching contributions of the sample are due to the local temperature rising at the surface layers and to the presence of photochemical effects inherent to the interaction with the environment inside the chamber during irradiation.

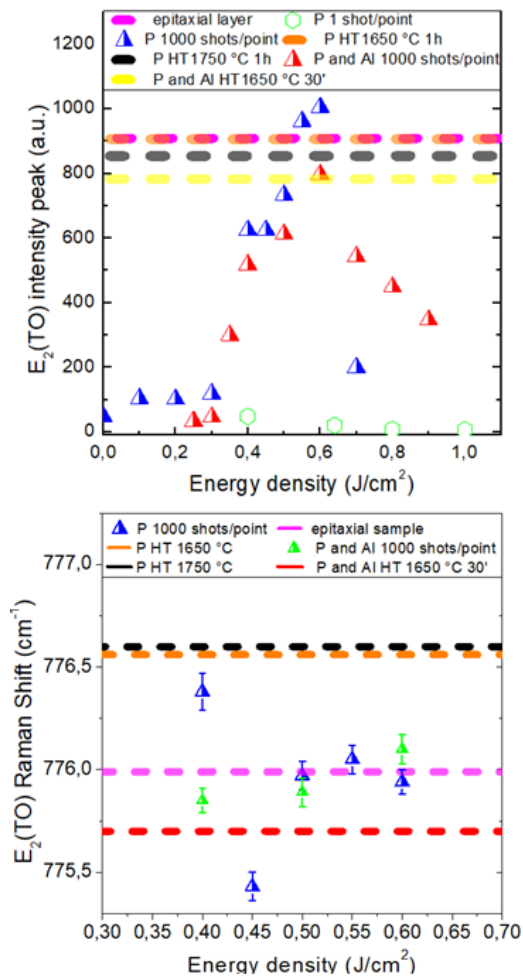


Figure 1: a) Raman  $E_2(TO)$  intensity peak and b) Raman  $E_2(TO)$  vibrational mode frequency vs energy density for single source implant and double source and body implants.

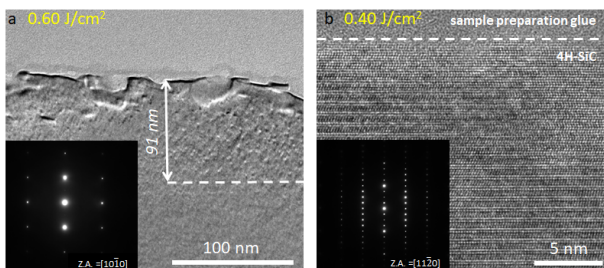


Figure 2: a) XTEM Bright field image of the 0.60  $J/cm^2$  laser annealed source implant. The inset shows the 4H-SiC diffraction pattern under [11-10] zone axis. b) HRTEM of the source implant sample subjected to 0.40  $J/cm^2$  laser fluence showing periodic ABAC stacking sequence acquired in correspondence of the surface under the [11-20] zone axis. The inset reports the related 4H-SiC diffraction pattern.

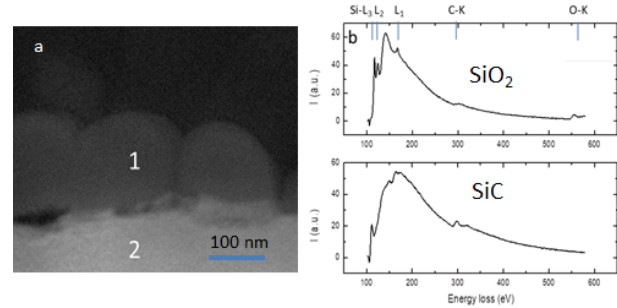


Figure 3: (a) STEM image of 0.40  $J/cm^2$  treated source implant surface and (b) electron energy loss spectroscopy (EELS) spectra coming from surface aggregates and from implanted area.)

## Conclusions

In this article the results of laser annealing related to implanted epitaxial layers with single P implantation and double P and Al implantations were compared with the single thermal annealing treatment. From the work presented here it is clear that the XeCl multi-laser pulses system is able to recover implantation damage. By observing the intensity variation of Raman phonon modes it was possible to plot crystal recovery trend as a function of energy density, from sub melting regime to phase separation. Laser pulse acting in a non-equilibrium regime and taking advantage of rapid annealing and cooling ramps is able to recover implantation damage generating a lower point defects concentration. Surface etching phenomena are due both to Si atoms desorption already known in conventional thermal annealing and to oxidation phenomena occurring inside the chamber in the presence of O. It is possible to affirm that laser annealing constitutes, with suitable precautions, a viable way as a post-implant thermal process.

## Acknowledgement

This research was funded by the ECSEL JU project Win-SiC4AP (Wide Band Gap Innovative SiC for Advanced Power), grant agreement n. 737483.

## References

- [1] SIMONKA, V.; TOIFL, A.; HÖSSINGER, A.; SELBERHERR, S.; WEINBUB, J.: *Transient model for electrical activation of aluminium and phosphorus-implanted silicon carbide*. J. Appl. Phys. 2018, 123, 325701.
- [2] OSVAY, M., RANOGAJEC-KOMOR, M.: *Hishida, Y.; Watanabe, M.; Nakashima, K.; Eryu, O.* Mater. Sci. Forum 2000, 873, 338–342.

- [3] AHMED, S.; BARBERO, C.J.; SIGMON, T.W. : *Activation of ion implanted dopants in  $\alpha$  SiC* Appl. Phys. Lett. 1995, 66, 712–714.
- [4] TANAKA, Y.; TANOUE, H.; ARAI, K. : *Electrical activation of the ion-implanted phosphorus in 4H-SiC by excimer laser annealing*. J. Appl. Phys. 2003, 93, 5934.
- [5] BOUTOPOULOS, C.; TERZIS, P.; ZERGIOTI, I.; KONTOS, A.G.; ZEKENTES, K.; GIANNAKOPOULOS, K.; RAPTIS, Y.S.: *Laser annealing of Al implanted silicon carbide: Structural and optical characterization*. Appl. Surf. Sci. 2007, 253, 7912–7916
- [6] MAZZAMUTO, F.; HALTY, S.; MORI, Y.: *Silicon Carbide recrystallization mechanism by non-equilibrium melting laser anneal*. Mater. Sci. Forum 2016, 858, 540–543.
- [7] NAKASHIMA, S.; AND HARIMA, H.: *Raman Investigation of SiC Polytypes*. Phys. Status Solidi 1997, 32, 162.
- [8] DUTTO, C.; FOGARASSY, E.; MATHIOT, D. : *Numerical and experimental analysis of pulsed excimer laser processing of silicon carbide*. Appl. Surf. Sci. 2003, 292, 362–366.
- [9] SUGIE, R.; UCHIDA, T.: *Determination of stress components in 4H-SiC power devices via Raman spectroscopy*. J. Appl. Phys. 2017, 122, 195703.
- [10] CALABRETTA, C.; ZIMBONE, M.; BARBAGIOVANNI, E.G.; BONINELLI, S.; PILUSO, N.; SEVERINO, A.; DI STEFANO, M.A.; LORENTI, S.; CALCAGNO, L.; LA VIA, F.;; *Thermal Annealing of high dose P implantation in 4H-SiC*. Mater. Sci. Forum 2019, 963, 399–402.
- [11] CALABRETTA, C.; AGATI, M.; ZIMBONE, M.; ET AL.: *Laser Annealing of P and Al implanted 4H-SiC epitaxial layers*. Materials 2019,12, 3362.
- [12] KIMOTO, T.; COOPER, J.A.: *Phase diagram for the interaction of oxygen with SiC*. Appl. Phys Lett. 2002, 81, 3061–3063.
- [13] SONG, Y.; SMITH, F.W. : *Measurement of Formation Cross Sections of Short-Lived Nuclei by 14 MeV Neutrons*. Report JAERI-M 92-020. Tokai-mura: Japan Atomic Energy Research Institute, 1992.

# Clinical scanners for wooden Cultural Heritage investigations: X-Ray Multislice Computed Tomography (MSCT) and Magnetic Resonance Imaging (MRI)

S. Longo<sup>1-2\*</sup>, S. Capuani<sup>2</sup>, E. Fazio<sup>1</sup>

<sup>1</sup>*Department of Mathematical and Computational Sciences, Physics Sciences and Earth Sciences (MIFT), University of Messina, Messina, Italy;*

<sup>2</sup>*NMR Laboratory, National Research Council-Institute for Complex Systems (CNR-ISC), Department of Physics Sapienza University of Rome, Roma, Italy.*

\*Corresponding Author email: [sveva.longo@unime.it](mailto:sveva.longo@unime.it)

## Abstract

Non-destructive and non-invasive approaches are fundamental for cultural heritage investigations. X-ray Computed Tomography (CT) and Nuclear Magnetic Resonance (NMR) are the most important imaging techniques in the medical field. In this work, new protocols for clinical Siemens CT based on multi-slice acquisition principle and Philips MRI clinical scanner suitable for cultural heritage wooden objects and archaeological waterlogged wood remains were developed. By clinical CT investigation, it is possible to obtain information about densities through Hounsfield Unit (HU) values measurements on Multi-Planar Reconstruction (MPR) images. By MRI, it is possible to obtain information about water content and conservation status by  $T_1$ ,  $T_2$  and  $T_2^*$  weighted images on waterlogged wood. Combining these two methods, a complete panorama on wooden conservation can be obtained.

**Keywords:** clinical scanners, wood analysis, conservation science, MSCT, MRI.

## Introduction

X-ray Computed Tomography (CT) and Nuclear Magnetic Resonance (NMR) are very widespread in the field of medicine, thanks to their characteristic of being able to observe internal parts of the human body without any injury to the patient. Although they are non-destructive diagnostic tools, the application to other fields outside medicine is nowadays well established [1, 2]. Both techniques are adaptable to wooden cultural heritage conservation science [3, 4]. This is possible thanks to some specific features of the same techniques, listed below, for the best-known case concerning biomedical applications. CT scan uses X-rays to make a detailed picture of bones or high densities structures inside the body. Instead, NMR is a spectroscopy that uses a magnetic field and radio wave pulses to make a picture of organs and soft tissue inside the body. CT images are a result of the different linear coefficient attenuation of human structures which are translated in 2001 shades of grey pixels. Instead, Nuclear Magnetic Resonance Imaging (MRI) can furnish the so-called “weighted images” representative of the spatial distribution of several NMR parameters. These parameters are the relaxation times  $T_1$ ,  $T_2$ ,  $T_2^*$  and molecular diffusion coefficient  $D$  of water protons inside tissues. Since wood is an organic material, it could be considered as human tissue and, therefore, CT-scan is used for dry

wood linear coefficient attenuation estimation and MRI analysis for waterlogged wood investigations.

In this work, clinical computed tomography, based on multi-slice acquisition principle (MSCT) and Nuclear Magnetic Resonance Imaging (MRI) were used to investigate different species of wood samples. It was possible by MSCT to obtain densities information through Hounsfield Unit Scale (HU), calibrated on attenuation coefficient  $\mu$ . All these values were collected and correlated with wood density values expressed in  $\text{Kg}/\text{m}^3$  obtained by the gravimetric method in order to validate the adopted methodology. It was possible by MRI to collect relaxometry data based on  $T_1$ ,  $T_2$  and  $T_2^*$  relaxation times of water inside each wood samples, in that way imbibition information was collected.

## Materials and Methods

### *Wood samples*

Sixteen cylinder-shaped samples of wood, each of 50 cm in length and 3 cm in diameter, were analysed (Tab. 1).

Wood species analysed
Poplar ( <i>Populus alba</i> )
Red Spruce ( <i>Picea abies</i> )
Silver Fir ( <i>Abies alba</i> )
Walnut ( <i>Juglans nigra</i> )
Oak ( <i>Quercus petraea</i> )
Maritime Pine ( <i>Pinus pinaster</i> )
Bahia ( <i>Mitragyna ciliata</i> )
Limba ( <i>Terminalia superba</i> )
Anigrè ( <i>Aningeria altissima</i> )
Sapelli ( <i>Entandrophragma cylindricum</i> )
Toona ( <i>Toona ciliata</i> )
African Walnut ( <i>Lovoa trichilioides</i> )

Table 1: *Wood nomenclature.*

### Imbibition

Imbibition was obtained by immersing samples in 5 l of distilled water. The container was covered with plastic wrap so that water does not evaporate, and dust particles do not contaminate the solution. To Accelerate the imbibition process, wood samples were boiled in order to let water penetrate into the log more easily, as reported in Ref [5].

### Multislice Computed Tomography (MSCT)

A Somatom Sensation 16 MSCT (Siemens Healthcare) with a gantry opening of 70 cm was used. The acquisition was performed setting the following parameters: 330 mAs, 120 kV, slice thickness of 0.75 mm. Images reconstructions Multi Planar Reconstruction (MPR) and Volume Rendering Technique (VRT) were obtained through SYNGO software by Siemens Leonardo Workstation. OsiriX software was used to analyse DICOM (Digital Imaging and Communications in Medicine) images and to obtain regions of interest (ROI). The working principle of the MSCT technique is based on the following mechanism. The X-ray attenuation is the reduction of the intensity of an X-ray beam as it traverses matter. The reduction may be caused by absorption or by deflection (scatter) of photons from the beam and can be affected by different factors such as beam energy and the atomic number of the absorber. It can be expressed as:

$$I = I_0 e^{-\mu E d}$$

where  $I$  is the emerging beam rays,  $I_0$  the incident beam rays;  $e$  is a constant (2.718);  $\mu E$  is the linear attenuation coefficient and  $d$  is the thickness of the material crossed. Knowing the values of  $I$  and  $I_0$ , you can calculate the value of  $\mu$ , which is the measured parameter of CT.

The linear coefficient attenuation ( $\mu$ ) depends on some parameters such as sample density and its atomic number  $Z$  as well as on the number of electrons per gram and the wavelength of the beam. Every material has its linear attenuation coefficient.

In order to obtain image reconstruction, CT image is divided in a squared surface called matrix, in which the pixel is the smallest unit and, because the section has a specific thickness, the voxel (volumetric picture element) corresponds to the volumetric unit. At each voxel, a numerical value is assigned corresponding to the average of the attenuation of the corresponding tissue volume, called the CT number or Hounsfield Unit (HU). In the CT Hounsfield Unit Scale bones density is expressed by values from +1000 HU; water density by 0 HU and air density by -1000 HU.

### Nuclear Magnetic Resonance Imaging (MRI)

A Philips Achieva 3.0 T X-series, equipped with a 3T static magnetic field, high-performing imaging gradients with an 80 mT/m maximum intensity with 200mT/m sloping ramp, and a FreeWave 32 SENSE-HEAD canals coil was used. T2 -weighted (T2-w) images were performed with a 5 mm slice thickness (STK) using a Multi echo sequence with Echo Time (TE) = 16 ms, Repetition Time (TR) =1500 ms. T2\*-weighted (T2\*-w) images were performed with STK= 5 mm and a Multi echo sequence with TE = 4 ms, TR = 1000 ms. T1-weighted (T1-w) images, an Inversion Recovery Turbo Spin Echo sequence was used with an STK= 3 mm, TE = 30 ms, Inversion recovery (IR) = 1800 ms, TR = 2000 ms. Wood species densities ( $d=M/V$ ) by the gravimetric method [5] were obtained for each wood specimens. Masses (M) of each wood sample were measured with an analytical balance BP211D Sartorius and volume (V) were calculated. Then the samples were dried inside the Universal Memmert Oven stove at the temperature of  $T = 103,5$  C for 24 hours. Then, the masses have been measured and this procedure has been repeated for a second time, in order to achieve 48 hours of drying time.

MRI is based on NMR spectroscopy. Because of nuclear paramagnetism, the macroscopic magnetization ( $M_0$ ) is generated when an object is put in a magnetic field ( $B_0$ ). An electromagnetic field in the radiofrequency (RF) range is used to stimulate the spins of hydrogen nuclei that are immersed in a strong static magnetic field to keep them away from the thermodynamic equilibrium condition. The NMR signal is generated by the return to equilibrium of the proton spin system. The RF stimulation moves the magnetization  $M_0$  from the direction parallel to  $B_0$  to the direction perpendicular to  $B_0$ . When the spins of the hydrogen nuclei are no longer stimulated, they return to their initial position, creating signals that are received by the RF probe as electromotive force. The intensity of the acquired NMR signal is proportional to the number of hydrogen spins in the volume investigated (spin density). Signal decays exponentially in time because of spin-spin and spin-lattice relaxation processes, which are quantified by the parameters  $T_1$  and  $T_2$  respectively. Images reconstruction is similar to computed tomographic scanners and the primary source of NMR images contrast is the spin density and the relaxation times  $T_1$  and  $T_2$ .

## Results and Discussion

In this work, we investigate the real possibility to use CT and NMR to characterize wood samples of different nature or under different atmospheric conditions to support, correlate or integrate structural and morphological information obtained with conventional spectroscopic techniques such as FTIR, Raman and SEM. MSCT images of some investigated wood samples were displayed (Fig. 1).

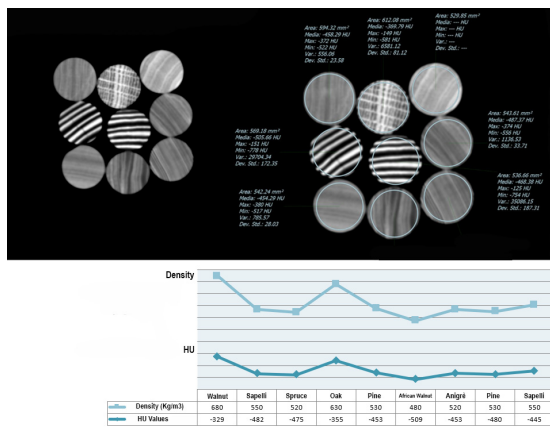


Figure 1: MSCT image

It is possible to observe that each wood has its radiopacity translated into shades of grey. HU values range between - 327 HU for walnut wood (*Junglans regia*) and - 646.5 HU for silver fir wood (*Abies alba*). Thus, if we generalise making it valid for the families to which these two kinds of wood belong, we can say that late-wood region (light voxels) has higher HU values than early-wood ones (dark voxels). These values agree with the typically known characteristic of wood: compared to springwood, latewood has more mass volume and strength as well as higher values of the parameters related to shrinkage and swelling [6]. Indeed, in terms of water absorption, early-wood ensures the rapid transport of the sap at the beginning of the vegetative season, while latewood formed in the summer is mainly due to support task. A further exciting trend found in the significant linear correlation between the HU values and the density ( $\text{Kg/m}^3$ ) of each wood (not shown). These results improve how MSCT is a valuable technique to understand not only implementation methods of a wooden object but also permit to obtain information about microstructure and density of the material and therefore its state of conservation. Unfortunately, by MSCT, it is not possible to have a clear idea about water-content, which is the leading cause of wood degradation. On the other hand, by MRI it is possible to have precise details about moisture and porosity of the wood.

MRI T2-weighted image and ROI's selection are shown in Fig. 2.

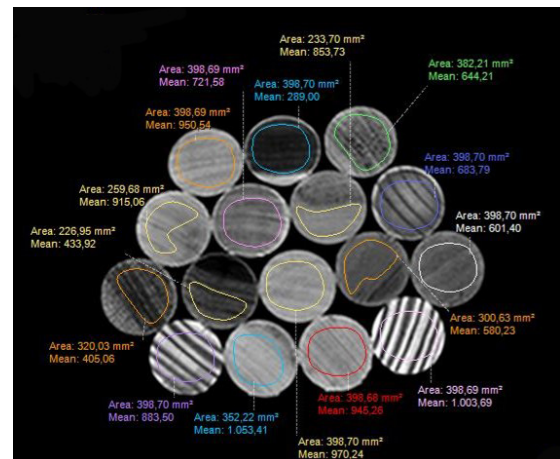


Figure 2: MRI image

Under the same conditions of imbibition, the  $T_1$ ,  $T_2$  and  $T_2^*$  relaxation times were measured. We remark that  $T_1$  and  $T_2$  relaxation times give information about microstructure due to the spin-spin relaxation process and free water-content due to the lattice-spin, respectively.  $T_2^*$  is a parameter which results principally from inhomogeneities in the main magnetic field. In our case,  $T_2^*$  values are included in a range from a minimum of about 2 ms for poplar wood (*Populus alba*) up to a maximum of about 25 ms for pinewood (*Pinus pinaster*).

$T_2$  times values recorded, ranging from a minimum of 10,7 ms for poplar (*Populus alba*) to a maximum of 51,5 ms for red spruce (*Picea abies*). Relaxation time  $T_1$  varies from a minimum of 81.6 ms for the silver fir (*Abies alba*) up to about 577 ms for sapelli wood (*Entandrophragma cylindricum*). Thus, early and latewood areas in tree-rings are clearly distinguished in terms of a significant difference in the relaxation times values. On the overall, in the latewood areas, the  $T_2$  values are lower concerning early-wood, indicating the presence of smaller vessel diameters [7] compared to those of springwood.

At this point, wood MSCT and MRI macroscopic characteristics were compared with macroscopic wood identification key [8] usually utilised by wood experts. We observe mainly that it is possible to distinguish between conifers and deciduous trees. In details: growth rings, multiple parenchymatic rays, ring-porous structure, texture, possible knots and plant defects, are visible. Ultimately, from the results obtained by MSCT and NMR scanners, information about the wood species, the porosity, the density of the material and the moisture content in a non-destructive and non-invasive way are obtained. All data are exciting for more in-depth cultural heritage investigations than state of the art.

## References

- [1] KAICK G. AND DELORME S.: *Computed tomography in various fields outside medicine*. Eur Radiol. 15 Suppl 4, D74-81 (2005)

- [2] BLUMICH B.: *NMR Imaging of Materials*. Clarendon Press, Oxford, 2003.
- [3] LONGO, S. ET AL.: *Investigation of an Egyptian Mummy board by Using Clinical Multi-slice Computed Tomography*. *Studies in Conservation*, **63**(7), 383–390 (2018).
- [4] BUCUR V.: *Nondestructive Characterization and Imaging of Wood* Springer Series in Wood Science, Berlin, 2003.
- [5] BONAMINI G. ET AL.: *Elementi di tecnologia del legno e utilizzazioni forestali*. Trento, 2004
- [6] GIORDANO G.: *Tecnologia del legno, Vol. I* UTET, Torino, 1988.
- [7] NARDI BERTI R.: *La struttura anatomica del legno ed il riconoscimento dei legnami italiani di più corrente impiego* CNR-IVALSA, Firenze, 2006.
- [8] WHEELER, E. A: *The InsideWood Database* <http://insidewood.lib.ncsu.edu/search>, Published on the Internet, 2004.

# Active Cooling with Optically Levitated Nanoparticles

F. Patti<sup>1,2,\*</sup>, R. Saija<sup>1,2</sup>, M. A. Iatì<sup>2</sup>, O. M. Maragò<sup>2</sup>

<sup>1</sup>*MIFT, Università di Messina, I-98156 Messina, Italy*

<sup>2</sup>*CNR-IPCF, Istituto per i Processi Chimico-Fisici, I-98158 Messina, Italy*

\*Corresponding Author email: [fpatti@unime.it](mailto:fpatti@unime.it)

## Abstract

The study of the behavior of a Brownian particle in the potential of an optical trap in a rarefied air, on which an active cooling system is switched on, is directly linked to issues as: where to start to see quantum behaviors on mesoscopic objects? [1] In fact these systems allow us to influence the temperature of the center of mass of the trapped nanoparticle by acting on some macroscopic parameter. The increasing sensitivity in the measurement of positions and velocity of nanoscopic objects allowed development of this field [2]. Unlike a particle trapped in a Fabry-Perot cavity, who "self-cools" because of the Doppler enhancement, in a active system, the laser power is modulated depending on the position and velocity of the particle, in order to reduce the temperature of the center of mass [3].

**Keywords:** laser cooling, optical tweezers, T-matrix formalis.

## Active Cooling with a Sphere

The starting point to reach our goal is to spend some words on the physical quantity that characterize the dynamics of the problem, namely the thermal noise, the resistance of the fluid and the external deterministic forces (if present) [4]. The latter, in our case, consists of the force of the optical tweezers and the feedback (FB) system and I'll talk about it later. The first two quantities are related to each other, from the fluctuation-dissipation theorem, and the diffusion coefficients (friction) can be defined for both the translational and the rotational motion, which are not the same among them [5]. Moreover, for symmetrical particles the diffusion coefficient (and therefore also the friction coefficient) is the same for all three degrees of freedom (translational or rotational, respectively).

The crucial step at this point is to write the equations of motion for each of the translational degrees of freedom. These equations must take into account that: the inertial term plays an important role, the particle is subject to the optical force of the tweezers, feedback is active. This FB term simulates the modulation of the power according to the position  $r$  and speed  $v_r$  of the particle, weighted by the FB constant  $\beta$ :

$$F_{feedback} = \beta \frac{rv_r}{\langle r \rangle_{\beta=0} \langle v_r \rangle_{\beta=0}} F_{RAY}$$

where in the denominator are present the positions and velocities average when the feedback is off,  $F_{RAY}$  is the optical force term. Another fundamental point is that the FB is the same for all three degrees of freedom: we chose to modulate the power by measuring speed and position

on the x axis.

## Forces in the T-Matrix formalism

To calculate the value of the force that appears in the equations, you need first determine the optical conditions of the system, then choose the refractive indices, the lens and the laser. Once we have chosen this parameters, we used the T-matrix formalism to calculate the optical forces on a grid centered in the focus of the lens, which is the region in which the dynamics develop [6]. Then we start the simulation and at each step of the dynamics, we look for the grid cell in which the particle mass center is located and the force value is calculated by linearising for each degree of freedom.

## Results

The main result of the simulation are the traces, that is the position of the particle as time changes. What about their shape? While at ambient pressure the particle's motion is dominated by the viscous force, the inertial force dominates in a vacuum of a few Pascal and the particle's motion becomes ballistic, so we expect sinusoidal profiles. [7] From their statistical study it is possible to obtain numerous and significant results.

In this report we show the most interesting and representative result, that is the shape of the potential. If you calculate it, you notice that it's sharper, on the degree of freedom on which the FB is turned on (figure 1).

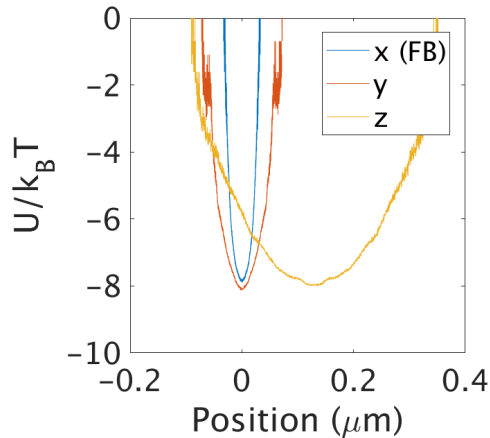


Figure 1: *Potential shape reconstructed from the distribution of positions along the three axes. The minimum of the curves is at the equilibrium position of the trap (zero force) and coincides with the nominal focus of the lens. The axial equilibrium position (along  $z$ ) is shifted from the nominal focus because of the increased scattering force. The width of the curve is related to the trap stiffness which is linked to the power of the laser.*

## Conclusion

More research is needed to clarify what, for example, is the formal relationship that links the temperature of the center of mass to the other parameters of the trap or medium. But as a first step, these results allow us on the one hand to be able to expand this cooling-T-matrix approach to core-shell objects, with arbitrary size parameters and refractive index and also to optically active particle[8], and on the other to think about more complicated situations, e.g. what happens when the object is no longer spherical [9, 10].

## References

- [1] ROMERO-ISART, O., JUAN, M. L., QUIDANT, R. AND CIRAC, J. I.: *Toward quantum superposition of living organisms.* . New J. Phys. 12, 033015 (2010).
- [2] LI, T., KHEIFETS, S., MEDELLIN, D. AND RAIZEN, M. G.: *Measurement of the instantaneous velocity of a Brownian particle.* . Science 328, 1673–1675 (2010).
- [3] LEVI P. NEUKIRCH AND A. NICK VAMIVAKAS: *Nano-optomechanics with optically levitated nanoparticles.* . Contemporary Physics, DOI: 10.1080/00107514.2014.969492
- [4] W. T. COFFEY, YU. P. KALMYKOV, J. T. WALDRON: *The Langevin Equation.* . World Scientific, Singapore, 2005
- [5] JONES, MARAGÒ AND VOLPE: *Optical Tweezers.* . Cambridge University Press, 2015
- [6] F. BORGHESE, P. DENTI, R. SAIJA: *Scattering from model nonspherical particles.* . Springer, Berlin, 2007
- [7] JAN GIESELER, BRADLEY DEUTSCH, ROMAIN QUIDANT AND LUKAS NOVOTNY: *Sub-Kelvin Parametric Feedback Cooling of a Laser-Trapped Nanoparticle.* . Phys. Rev. Lett. 109 (2012), 103603
- [8] F. PATTI, R. SAIJA, P. DENTI, G. PELLEGRINI, P. BIAGIONI, M. A. IATÌ, O. M. MARAGÒ : *Chiral optical tweezers for optically active particles in the T-matrix formalism* Scientific Reports volume 9, Article number: 29 (2019)
- [9] J. PERRIN: *Mouvement Brownien d'un ellipsoïde-I.* . Ann. Chimie Physique, 18, 5-114
- [10] FERDINANDO BORGHESE, PAOLO DENTI, ROSALBA SAIJA, MARIA ANTONIA IATÌ: *Optical trapping of nonspherical particles in the T-matrix formalism.* . 17 September 2007 / Vol. 15, No. 19 / OPTICS EXPRESS 11984

# Interaction of Mechanical Oscillators by means of the quantum vacuum

A. Settineri<sup>1,\*</sup>, O. Di Stefano<sup>2</sup>, S. Savasta<sup>1</sup>

<sup>1</sup>*Dipartimento di Scienze Matematiche e Informatiche, Scienze Fisiche e Scienze della Terra, Università di Messina, I-98166 Messina, Italy*

<sup>2</sup>*Theoretical Quantum Physics Laboratory, RIKEN Cluster for Pioneering Research, Wako-shi, Saitama 351-0198, Japan*

\*Corresponding Author email: [alessiosettineri@hotmail.it](mailto:alessiosettineri@hotmail.it)

## Abstract

Two close parallel mirrors attract due to a small force (Casimir effect) originating from the quantum vacuum fluctuations of the electromagnetic field. These vacuum fluctuations can also induce motional forces exerted upon one mirror when the other one moves. Here we consider an optomechanical system consisting of two vibrating mirrors constituting an optical resonator. We find that motional forces can determine noticeable coupling rates between the two spatially separated vibrating mirrors. We show that, by tuning the two mechanical oscillators into resonance, energy is exchanged between them at the quantum level [1]. This coherent motional coupling is enabled by the exchange of virtual photon pairs, originating from the dynamical Casimir effect. The process proposed here shows that the electromagnetic quantum vacuum is able to transfer mechanical energy somewhat like an ordinary fluid.

**Keywords:** Quantum Optomechanics, Ultra-Strong Coupling, Quantum Vacuum, Dynamical Casimir Effect, Virtual Photon Pairs.

## Introduction

Effective interactions able to coherently couple spatially separated qubits are highly desirable for any quantum computer architecture. Very recently, it has been shown that the exchange of virtual photons between artificial atoms can give rise to effective interactions of multiple spatially-separated atoms [2], opening the way to vacuum nonlinear optics. Given this result, one may wonder whether it is possible for spatially separated mesoscopic or macroscopic bodies to interact at a quantum level by means of the vacuum fluctuations of the electromagnetic field. It is known that, owing to quantum fluctuations, the electromagnetic vacuum is able, in principle, to affect the motion of objects through it, like a complex fluid [3]. For example, it can induce dissipation and decoherence effects on the motion of moving objects. By using linear dispersion theory, it has also been shown that vacuum fluctuations can induce motional forces exerted upon one mirror when the other one moves. Here we show that two spatially separated moveable mirrors, constituting a cavity-optomechanical system, can exchange energy coherently and reversibly, by exchanging virtual photon pairs. Our results show that *the electromagnetic quantum vacuum is able to transfer mechanical energy somewhat like an ordinary fluid*. It would be as if the vibration of a string (mechanical oscillator 1) could be transferred to the membrane of a microphone (mechanical oscillator 2) in the absence of air (or any excited medium filling the

gap).

## Model

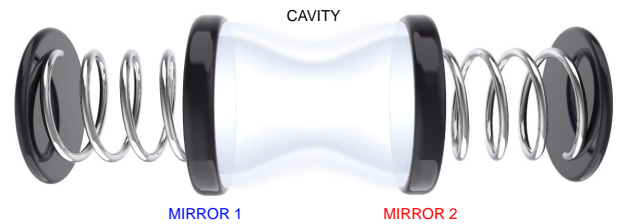


Figure 1: *Schematic of an optomechanical system constituted by two vibrating mirrors. If one of the two vibrating mirrors is excited, its excitation can be transferred coherently and reversibly to the other mirror. The interaction is mediated by the exchange of virtual photon pairs.*

We consider a system constituted by two vibrating mirrors interacting via radiation pressure [see Fig. 2]. Both the cavity field and the position of the mirrors are treated as dynamical variables and a canonical quantization procedure is adopted [4]. By considering only one mechanical mode for each mirror, with resonance frequency  $\omega_i$  ( $i = 1, 2$ ) and bosonic operators  $\hat{b}_i$  and  $\hat{b}_i^\dagger$ , the displacement operators can be expressed as  $\hat{x}_i = X_{\text{zpf}}^{(i)}(\hat{b}_i^\dagger + \hat{b}_i)$ ,

where  $X_{zpf}^{(i)}$  is the zero-point-fluctuation amplitude of the  $i$ th mirror. The mirrors form a single-mode optical resonator with frequency  $\omega_c$  and bosonic photon operators  $\hat{a}$  and  $\hat{a}^\dagger$ . The system Hamiltonian can be written as  $\hat{H}_s = \hat{H}_0 + \hat{H}_I$ , where ( $\hbar = 1$ )  $\hat{H}_0 = \omega_c \hat{a}^\dagger \hat{a} + \sum_i \omega_i \hat{b}_i^\dagger \hat{b}_i$  is the unperturbed Hamiltonian. The mirror-field interaction Hamiltonian can be written as  $\hat{H}_I = \hat{V}_{om} + \hat{V}_{DCE}$ , where  $\hat{V}_{om} = \hat{a}^\dagger \hat{a} \sum_i g_i (\hat{b}_i + \hat{b}_i^\dagger)$  is the standard optomechanical interaction conserving the number of photons,  $\hat{V}_{DCE} = (1/2)(\hat{a}^2 + \hat{a}^{\dagger 2}) \sum_i g_i (\hat{b}_i + \hat{b}_i^\dagger)$  describes the creation and annihilation of photon pairs, and  $g_i$  is the optomechanical coupling rate for mirror  $i$ . The linear dependence of the interaction Hamiltonian on the mirror operators is a consequence of the usual small-displacement assumption [4].

When describing most of the optomechanics experiments  $\hat{V}_{DCE}$  is neglected. This is a very good approximation when the mechanical frequency is much smaller than the cavity frequency (which is the most common experimental situation). However, when the mechanical frequencies  $\omega_i$  are on the order of the cavity-mode resonance frequency, are of the order of  $\omega_c$ ,  $\hat{V}_{DCE}$  cannot be neglected. We are interested in studying this regime, which can be achieved using microwave resonators and ultra-high-frequency mechanical micro- or nano-resonators. In order to properly describe the system dynamics, including external driving and dissipation, the coupling to external degrees of freedom needs to be considered. Dissipation and decoherence effects are taken into account by adopting a master-equation approach. For strongly coupled hybrid quantum systems, the description offered by the standard quantum-optical master equation breaks down [5, 6].

## Results

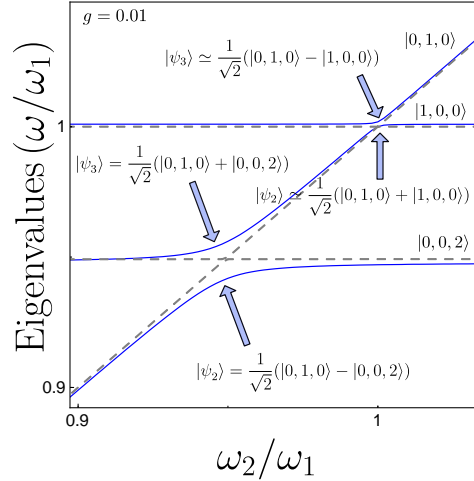


Figure 2: Relevant energy levels of the system Hamiltonian  $\hat{H}_s$  as a function of the ratio between the mechanical frequency of mirror 2 and that of mirror 1. An optomechanical coupling  $g/\omega_1 = 0.03$  has been used; the cavity-mode resonance frequency is  $\omega_c = 0.495\omega_1$ . The lowest energy anticrossing corresponds to the resonance condition for the DCE. The higher energy one is the signature of the mirror-mirror interaction mediated by the virtual DCE photons.

We begin our analysis by numerically diagonalizing the Hamiltonian  $\hat{H}_s$  in a truncated finite-dimensional Hilbert space. The blue solid curves in Fig. 2 describe the energy levels of the total Hamiltonian  $\hat{H}_s$  (including  $\hat{V}_{DCE}$ ) as a function of  $\omega_2/\omega_1$ . For the optomechanical couplings, we use  $g_1 = g_2 = g = 0.01\omega_1$ . The cavity-mode resonance frequency is fixed at  $\omega_c = 0.495\omega_1$ . This value is chosen close to the resonance condition for the DCE [7] in order to increase the effective coupling between the mirrors. For comparison, we also show in Fig. 2 (dashed grey lines) energy levels of the standard optomechanics Hamiltonian  $\hat{H}_0 + \hat{V}_{om}$ . The higher energy splitting in Fig. 2 originates from the coherent coupling of the zero-photon states  $|1, 0, 0\rangle$  and  $|0, 1, 0\rangle$ . At the minimum energy splitting the resulting states are well approximated by  $|\psi_{3,4}\rangle \simeq (1/\sqrt{2})(|1, 0, 0\rangle \pm |0, 1, 0\rangle)$ . This mirror-mirror interaction is a result of virtual exchange of cavity photon pairs. When the mirrors have the same resonance frequency, an excitation in one mirror can be transferred to the other by virtually becoming a photon pair in the cavity, thanks to the DCE. The resulting minimum energy splitting provides a measure of the effective coupling strength between the two mirrors.

We now investigate the system dynamics starting from a low-temperature thermal state and introducing the excitation of mirror 1 by a single-tone continuous-wave mechanical drive  $\mathcal{F}_1(t) = \mathcal{A} \cos(\omega_d t)$ .

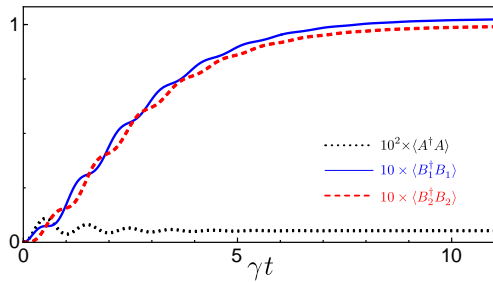


Figure 3: *System dynamics for  $\omega_c \simeq 1.5\omega_1$  under continuous-wave drive of mirror 1. The blue solid and red dashed curves describe the mean phonon numbers  $\langle \hat{B}_1^\dagger \hat{B}_1 \rangle$  and  $\langle \hat{B}_2^\dagger \hat{B}_2 \rangle$ , respectively, while the black dotted curve describes the mean intracavity photon number  $\langle \hat{A}^\dagger \hat{A} \rangle$  arising due to the DCE.*

We numerically solve the master equation for hybrid quantum systems in a truncated Hilbert space [6]. Figure 3 shows the time evolution of the mean phonon numbers of the two mirrors  $\langle \hat{B}_i^\dagger \hat{B}_i \rangle$  and the intracavity mean photon number  $\langle \hat{A}^\dagger \hat{A} \rangle$ . Here  $\hat{A}, \hat{B}_i$  are the *physical* photon and phonon operators. Such operators  $\hat{O} = \hat{A}, \hat{B}_i$  can be defined in terms of their bare counterparts  $\hat{o} = \hat{a}, \hat{b}_i$  as [8, 9]  $\hat{O} = \sum_{E_n > E_m} \langle \psi_m | (\hat{o} + \hat{o}^\dagger) | \psi_n \rangle | \psi_m \rangle \langle \psi_n |$ . We consider the system initially in the ground state. During its time evolution. We use  $\gamma_1 = \gamma_2 = \gamma = \omega_1/260$  and  $\kappa = \gamma$  for the mechanical and photonic loss rates. We consider a weak ( $\mathcal{A}/\gamma = 0.95$ ) resonant excitation of mirror 1 ( $\omega_d = \omega_1$ ). We present results for a normalized coupling strengths  $g/\omega_1 = 0.03$ , and set  $\omega_2 = \omega_1$ . The results shown in Fig. 3 demonstrate that the excitation transfer mechanism via virtual DCE photon pairs, proposed here, works very well for  $g/\omega_1 = 0.03$ . In steady state, mirror 2 reaches almost the same excitation intensity as the driven mirror 1. Performing simulation considering the interaction of the system with non-zero temperature reservoirs we also found that the influence of temperature on the mechanical expectation values is almost negligible. On the contrary, the cavity mode at lower frequency is much more affected by the temperature. We observe that for  $g/\omega_1 = 0.01$ , although the transfer is reduced, the effect is still measurable.

## Conclusions

In conclusion, we demonstrated that mechanical quantum excitations can be coherently transferred among spatially-

separated mechanical oscillators, through a dissipationless quantum bus, due to the exchange of virtual photon pairs. Furthermore, we demonstrated that this system can be used as a parametric down-converter [10]. The experimental demonstration of these processes would show that the electromagnetic quantum vacuum is able to transfer mechanical energy somewhat like an ordinary fluid. The results presented here open up exciting possibilities of applying ideas from fluid dynamics in the study of the electromagnetic quantum vacuum. Furthermore, these results show that the DCE in high-frequency optomechanical systems can be a versatile and powerful new resource for the development of quantum optomechanical technologies.

## References

- [1] O. DI STEFANO: *Interaction of Mechanical Oscillators Mediated by the Exchange of Virtual Photon Pairs*. Physical Review Letters, 2019.
- [2] R. STASSI: *Quantum nonlinear optics without photons*. Physical Review A, 2017.
- [3] M. KARDAR: *The “friction” of vacuum, and other fluctuation-induced forces..* Review of Modern Physics, 1999.
- [4] C. K. LAW: *Interaction between a moving mirror and radiation pressure: A Hamiltonian formulation*. Physical Review A, 1995.
- [5] F. BEAUDOIN: *Dissipation and ultrastrong coupling in circuit QED*. Physical Review A, 2011.
- [6] A. SETTINERI: *Dissipation and thermal noise in hybrid quantum systems in the ultrastrong coupling regime*. Physical Review A, 2011.
- [7] V. MACRÍ: *Deterministic quantum nonlinear optics with single atoms and virtual photons*. Physical Review X, 2017.
- [8] A. RIDOLFO: *Photon Blockade in the Ultrastrong Coupling Regime*. Physical Review Letters, 2012.
- [9] A. SETTINERI: *Conversion of Mechanical Noise into Correlated Photon Pairs: Dynamical Casimir effect from an incoherent mechanical drive*. Physical Review A, 2019.
- [10] A. F. KOCKUM: *Frequency conversion in ultrastrong cavity QED*. Scientific Reports, 2017.

REPORTS  
STUDENTI DI DOTTORATO DI  
RICERCA  
CICLO XXXIV

# Advanced processing for Silicon Nano-Wire based Solar Cells

G. Borgh<sup>1,\*</sup>, C. Bongiorno<sup>2</sup>, E. Fazio<sup>1</sup>, A. La Magna<sup>2</sup>, G. Mannino<sup>2</sup>, F. Neri<sup>1</sup>, S. Scalese<sup>2</sup>, R. A. Puglisi<sup>2</sup>

<sup>1</sup>*Department of mathematics and Computer Science, Physics and Earth Science (MIFT), University of Messina, Viale F. Stagno d'Alcontres, 31, 98166 Messina, Italy*

<sup>2</sup>*Consiglio Nazionale delle Ricerche (CNR) Istituto per la Microelettronica e Microsistemi (IMM), Strada Ottava 5, Zona Industriale, 95121 Catania, Italy*

\*Corresponding Author email: [gborgh@unime.it](mailto:gborgh@unime.it)

## Abstract

Silicon nanowires (Si-NWs) arrays show better optical properties compared to planar Si, fundamental aspect in the photoconversion process for efficient solar cells. In this work wires with diameters ranging from 3 to a few dozen nanometers were grown by the vapor-liquid-solid (VLS) mechanism. The metal catalysts chosen, gold, by far preponderant in literature and an innovative one i.e. tin, were deposited via sputtering onto Si substrates. The growth was carried out with an Inductively Coupled Chemical Vapor Deposition (IP-CVD) system. An efficient post growth gold removal procedure has been developed as gold residuals worsens the electrical properties of photovoltaic devices. Several investigation techniques including SEM, TEM, EFTEM, XPS have been used for the materials characterization

**Keywords:** nanowires, catalytic growth, etching, VLS, CVD, gold, tin.

## Introduction

Si-NWs are excellent building blocks for new generations of electronic and photonic devices like transistors [1], solar cells [2] and many others [3] because their dimensions such as diameter or length, their morphology and consequently their electronic properties can be controlled during synthesis in a predictable manner when using a suitable technique. VLS is the most widely used mechanism to obtain these nanostructures and it is known that gold (Au) is by far the most studied metal catalyst for VLS growth [4]. But although it brings many advantages, Au has relevant drawbacks. The main-one is that it introduces defects in the semiconductor electronic structure by generating localized trap states causing the devices electrical performance degradation [5]. Thus it is necessary to develop a high efficiency post growth Au removal method. So we firstly focused on setting up a removal procedure of Au from Si-NWs [6]. Therefore the possibility of replacing the metal catalyst with another one that is equally suitable was investigated, in order to maintain the advantages of the VLS mechanism but overstepping the drawbacks of Au. Among all metal candidates to replace it, tin (Sn) was chosen because it brings several advantages, including inexpensiveness and greater abundance in nature than Au; it also has a lower melting temperature which translates into energy savings and does not significantly alter the structure of the Si band gap.

## Materials and Methods

The substrates, specimens of 13 ohm-cm p-type Czochralski Si <100> and <111> of 1 cm<sup>2</sup> area, have preliminarily undergone to a cleaning procedure, based on sonication steps into different solvents and subsequent HF dip. Once the substrates were dried, the Au and Sn dots were sputtered onto them until an equivalent thickness of 2 nm and 2.3 nm, for Au and Sn respectively, was deposited. Depositions were carried out with a base pressure equal to 5x10<sup>-3</sup> mbar, 10 mA of current, for about a few tens of seconds. As soon as the deposition was completed, the substrates were inserted into the IP-CVD reactor for the Si-NWs growth. At this point the substrates were heated at 380 °C for 1 h then the deposition has been performed with the following process parameters: 20 mTorr pressure, process time 30 min, plasma power 20 W, gas ratio of SiH/Ar = 30 and substrate temperature of 380°C. The whole preparation was carried out in sequence. Various investigation techniques have been used for the systems characterization. Scanning electron microscopy (SEM) and transmission electron microscopy (TEM) to obtain morphological information such as nanostructures geometry, density and dimensions. Most of the time, SEM and TEM analyzes were performed immediately after CVD growth in order to minimize the alterations of the samples due to the exposure to the atmosphere. Qualitative chemical informations, was obtained by energy filtered electron

spectroscopy (EFTEM) and x-ray emission spectroscopy (XPS).

## Results and discussion

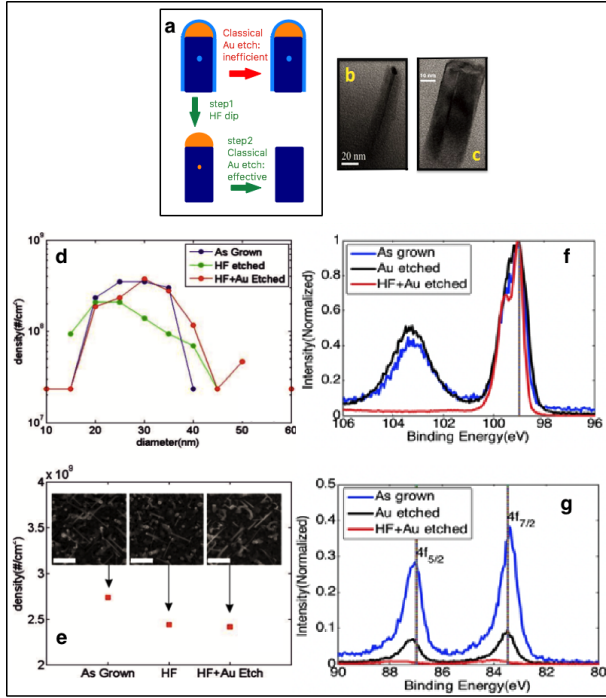


Figure 1: (a) Schematics illustrating the classical Au etching process (one step) and the two-step process developed. Insets: cross-sectional view TEM micrographs of Si-NWs after the Au removal single step (b), and after the two-steps Au etching (c). (d) Si-NWs density as a function of diameter is reported for as grown sample (blue circles), after the HF etching (green circles) and after HF+Au etching (red circles). (e) Average Si-NWs surface density for the three cases under study. The inset shows the relative SEM micrograph in planar view scale markers corresponds to 400 nm. High Resolution XPS spectra of the (f) Si 2p and (g) Au 4f of the as grown NWs (blue line), the sample obtained after the Au etching (black line) and the sample obtained after the two steps procedure (red line).

To prevent the devices electrical properties deterioration it is necessary to remove Au residuals after the NWs growth but the process stated in the literature, that involves a chemical bath of the samples into a Au etching solution (Fujifilm GOLD ETCH II with OHS, containing sodium iodide (NaI) and iodine (I<sub>2</sub>), diluted in H<sub>2</sub>O (1:10)) for a few minutes, results ineffective. TEM micrograph acquired for a NW after this procedure (fig. 1d) reveals indeed that the Au seed is still present atop the NW after the treatment. The reason for this inefficiency

is due to the presence of a SiO<sub>2</sub> film surrounding the Au cluster that is in turn due to the behavior of Au-Si eutectic system. It is known that Si dissolves in the metal during heating, but afterwards it migrates towards the Au/vacuum interface which is warmer than the Au/sub. interface due to an anisotropic eutectic cooling. The result is the formation of a Si layer that encapsulates the metal with an almost perfect isotropy; the following system air exposure leads its oxidation and a SiO<sub>2</sub> conformal coat surrounding Au is produced [7]. This SiO<sub>2</sub> shell hinders the removal of metal seeds by acting as passivating layer against the classical etching solution. For this reason we focused on developing a new protocol with high Au removal efficiency; specifically the defined procedure consists of two steps: 1) removing the passivating SiO<sub>2</sub> shell produced on the Si-NWs and on the Au tips by dipping for 5 min the specimens into a HF buffered solution diluted in H<sub>2</sub>O (1:10); 2) removing Au by dipping the samples for 4 min into the commercial Au etching solution mentioned above [6]. Figure 1a shows a schematization of the single step Au removal process and the process, based on two steps, that we developed. The result on the samples that have undergone to the two steps procedure is shown in fig. 1c in which no Au is detected. In order to evaluate the etching effect on the morphology the Si-NWs density has been monitored through SEM analysis (fig 1e). The results for the three samples i.e. as grown (blue circles), single etching step with HF (green circles) and the double step with HF+Au (red cycles), are reported in Figure 1d. As it is clear, no significant difference is evident between the distribution of the as deposited case and after the etching steps. Figure 1e shows that the density remains almost constant. This indicates that the morphology of the samples is maintained unaltered after the chemical reaction. XPS spectra of the Si 2p and Au 4f of the as grown NWs (blue line), the sample obtained after the Au etching (black line) and the sample obtained after the two steps procedure (red line) are reported in fig.1 f-g respectively. A peak centered at 103.5 eV revealing the presence of the SiO<sub>2</sub> that is detected in the spectra of both the as grown and in that obtained after the single step Au etching sample. The SiO<sub>2</sub>/Si intensity ratio is quite comparable in the two spectra thus indicating that the removal process does not affect the surface composition of the oxidized Si-NWs. The use of HF in the double step procedure (HF+Au-etching), allows to almost completely remove the SiO<sub>2</sub> as emerges from the figure 1f-red curve. The Au XPS region shown in Figure 1g indicates a significant decrease of the Au percentage for the sample subjected to the developed treatment compared to both those who underwent classical etching and as grown, confirming the effectiveness of the implemented process. The high efficiency in terms of percentage is shown in table 1: the Au residue in the samples subjected to the two-step procedure is less than 0.1 percent [6].

XPS data	As grown	Au etching	HF+Au etch.
Au	2,4	0,4	<0,1

Table 1: XPS Atomic percentage of Au as revealed in the NW samples.

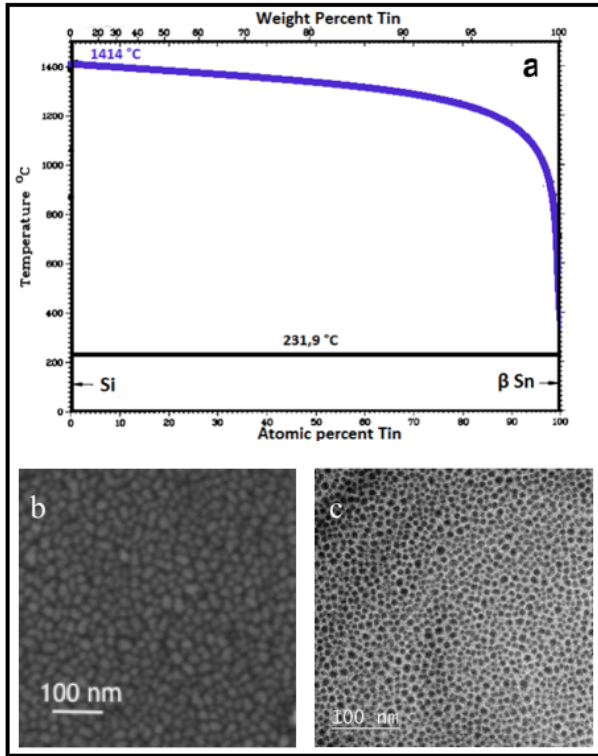


Figure 2: (a) Binary phase diagram of the Sn-Si system. Plan view micrographs (b) SEM and (c) TEM of tin catalyst after sputter deposition.

The experimental activity has also been devoted to the replacement of Au with Sn as a catalyst. Sn was chosen as a substitute to Au for its advantages with respect to Au: the eutectic temperature of the Sn/Si system is 232 °C [8], less than the eutectic temperature of the Si/Au system (363 °C)[9], that implies a lower thermal budget; Sn does not generate trap states into the semiconductor so no removal step is necessary; the Si solubility in Sn is  $10^5$ - $10^6$  times lower than in the Au [8], as indicated by the Si-Sn phase diagram shown in Figure 2a, which results in faster kinetic and into a precursors saving. Fig. 2b and 2c respectively show plan-SEM and plan-TEM micrographs of a typical Sn catalyst used for the CVD-VLS growth. The presence of Sn dots of about 20 nm large is clearly visible in both images with a strict dispersion of the size, indispensable requirement since it is the size of the catalyst dot that mainly determines the wires diameter.

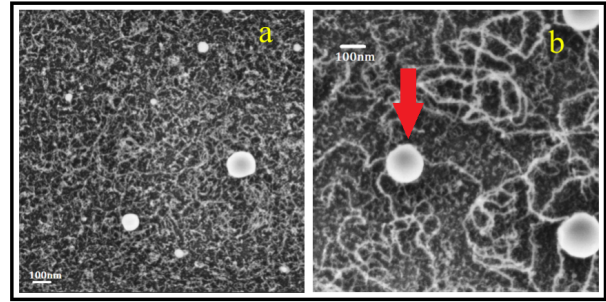


Figure 3: Plan view SEM micrographs of Si-NWs after Sn-catalyzed IP-CVD growth at (a) low and (b) high magnification.

Fig. 3 a and b show two SEM micrographs at different magnifications, acquired immediately after the CVD deposition. It is possible to observe the presence of nano filiform structures with a diameter between 10 and 20 nm and a length of several hundred nanometers. The big spherical (one indicated by the red arrow fig. 3b) placed on top of NWs array are composed of Sn as confirmed by EDX analyzes (not reported here). Its formation can probably take place during the sputtering deposition or during heating as a coalescence of smaller drops.

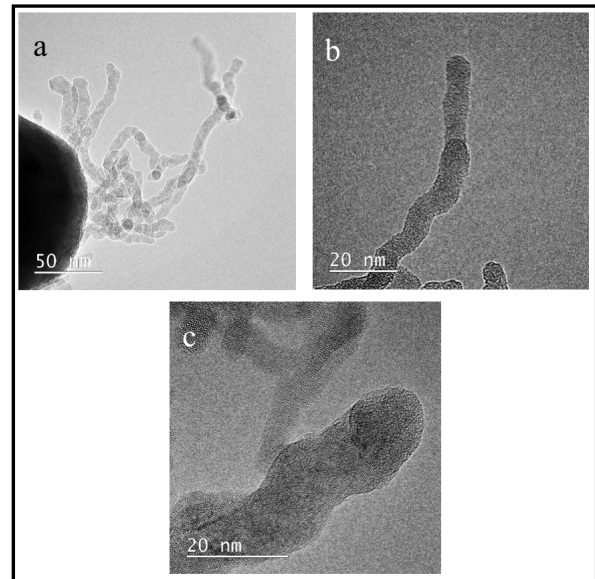


Figure 4: HR-TEM micrographs of (a) a group of tangled Si-NWs, (b) a single Si-NW from the group and (c) the same Si-NW showed in b at high magnification g.

In HRTEM micrographs reported in fig.4 a, b and c, we observe the presence of Si nano wires in which it is clearly possible to distinguish the crystalline planes so we can reasonably concluded that NWs are of polycrystalline nature.

ture. Therefore the nanostructures are composed of crystalline and not oxidized Si (see fig 5a-c). This result is promising, because the silicon wires, and not SiO<sub>2</sub> ones, are suitable for applications in microelectronics, thanks to their remarkable electro-optical properties. The diameter of the structures is almost uniform throughout the length and does not exceed 20 nm, many have a diameter less than 10 nm. Some structures exceed 800 nm in length. The polycrystalline structure is a consequence of the particular growth kinetics which does not occur according to a fixed crystallographic direction throughout the process, but varies continuously, resulting in a "worm-like" appearance of the nano-structures. The NWs obtained are coated with a uniform amorphous film of about 1.5 nm thick, a dimension in line with the typical thickness of native SiO<sub>2</sub> produced by oxidation following exposure to air. This data is confirmed by the EF-TEM images, shown in fig. 5, acquired at 26 eV for the SiO<sub>2</sub> (5b and 5d, bulk plasmon of SiO<sub>2</sub>), while those acquired at 17 eV for the Si (5a and 5c Si bulk plasmon), confirm that the core is composed of Si. These results are promising because a complete oxidation of the nano-systems can be excluded.

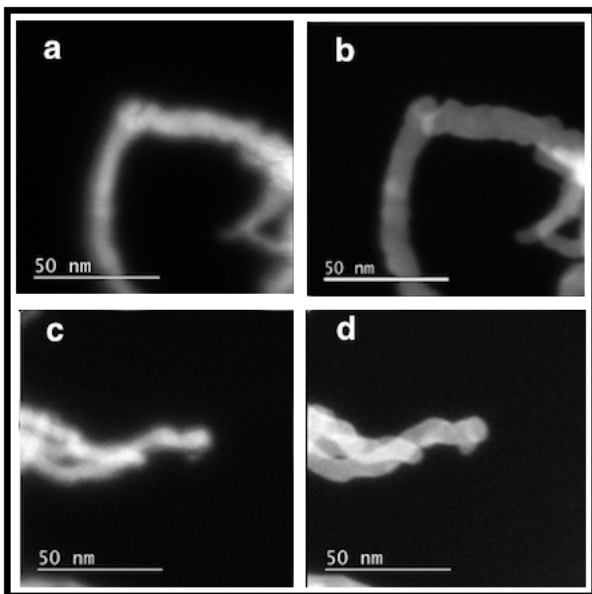


Figure 5: Energy Filtered TEM images of Sn-catalyzed Si-NWs acquired at 17eV (a and c) and 24 eV (b and d).

## Conclusions

In this work Si-NWs have been synthesized and studied as structures for the silicon surface engineering for

photovoltaic applications by virtue of their remarkable optical properties. The synthesis occurred through the IP-CVD technique by the well-known VLS mechanism. The metals investigated as catalysts were gold, the most widespread in the literature and tin, cheaper and less problematic than the previous one but exploited so far only little. We decided to use sputtering among all the techniques available for their deposition. The synthesis carried out using gold, as expected, produced nanowires straight, with a homogeneous morphology over the entire sample area. The Si-NWs obtained using tin as a catalyst present instead a worm-like morphology. Despite their morphology it is not yet optimized these preliminary results are encouraging because the obtained Si-NWs show a polycrystalline silicon structure in the core and are not completely oxidized, an essential property for electronic applications. For this reason we will proceed with the modulation of the process parameters in order to obtain morphologically optimized silicon nano-wires tin-catalyzed.

## References

- [1] Y. CUI, Z. ZHONG, D. WANG, W.U. WANG, C.M. LIEBER : *High performance silicon nanowire field effect transistors..* Nano Lett. 3 (2003) 149–152.
- [2] R.A. PUGLISI ET AL.: *Molecular doping applied to Si nanowires array based solar cells.* Solar Energy Materials and Solar Cells 132 (2015) 118–122 .
- [3] M. S. GUDIKSEN, L. J. LAUHON, J. WANG, D. C. SMITH, AND C. M. LIEBER,: *Growth of nanowire superlattice structures for nanoscale photonics and electronics.* Nature, vol. 415, no. 6872, pp. 617–620, 2002
- [4] WAGNER RS, ELLIS WC: *Vapor-Liquid-Solid mechanism of single crystal growth.* Appl.Phys Lett. 1964, 4: 89.
- [5] BULLIS WM: *Properties of gold in silicon.* Solid-State Electron.1966, 9(2): 97.
- [6] R.A. PUGLISI ET AL.: *Study on the Physico-Chemical Properties of the Si Nanowires Surface.* Nanomat. 2019, 9, 818.
- [7] RESSEL, B.; PRINCE, K.C.; HEUN, S.; HOMMA, Y. : *Wetting of Si surfaces by Au-Si liquid alloys.* Appl. Phys. 2003, 93, 3886.
- [8] R.W. OLESINSKI AND G. J. ABBASCHIAN: *The Si-Sn (Silicon-Tin) System.* Bulletin of Alloy Phase Diagrams Vol. 5 No. 3 1984.
- [9] H. OKAMOTO AND T. B. MASSALSKI: *The Au-Si (Gold-Silicon) System.* Bulletin of Alloy Phase Diagrams Vol. 4 No. 2 1983.

# Effect of Extended Practice on Adaptation to Virtual Surgeries

S. Gurgone<sup>1,\*</sup>, V. Venuti<sup>1</sup>, D. Borzelli<sup>2</sup>, P. de Pasquale<sup>3</sup>, M. Mezzetti<sup>4</sup>, D. J. Berger<sup>5</sup>, G. Aciri<sup>2</sup>, A. d'Avella<sup>2</sup>

<sup>1</sup>*Department of Mathematical and Computer Sciences, Physical Sciences, and Earth Sciences, University of Messina, Messina, Italy*

<sup>2</sup>*Department of Biomedical and Dental Sciences and Morphofunctional Imaging, University of Messina, Messina, Italy*

<sup>3</sup>*Laboratory of Neuromotor Physiology, IRCCS Fondazione Santa Lucia, Rome, Italy*

<sup>4</sup>*Department of Economics and Finance, University Tor Vergata, Rome, Italy*

<sup>5</sup>*Centre of Space Bio-Medicine and the Department of Systems Medicine, University of Rome Tor Vergata, Rome, Italy*

\*Corresponding Author email: [sgurgone@unime.it](mailto:sgurgone@unime.it)

## Abstract

It has been proposed that the Central Nervous System simplifies motor control by recruiting muscles in fixed groups or muscle synergies. In a previous study, support for this hypothesis has come from the demonstration that, in a single experimental session of virtual reaching task with myoelectric control, it is impossible to learn novel muscle activation patterns if they cannot be generated by the combination of synergies. In this study, we investigated whether longer practice of the same task, performed in three sessions over consecutive days, allows to learn new muscle synergies.

**Keywords:** virtual surgeries, electromyography, myoelectric control, muscle synergy, multiday learning, motor adaptation.

---

## Introduction

The redundancy of the motor system, i.e. the larger number of control variables in the musculoskeletal system with respect to the number of its degrees of freedom, leads to the outstanding question on how the Central Nervous System (CNS) selects one of the virtually infinite possible solutions to perform a task.

It has been proposed that the CNS recruits muscles in fixed groups or modules (i.e. muscle synergies), which are combined flexibly to perform different conditions of a task. The existence of muscle synergies has been investigated during many different tasks. Initially, evidence for synergies has come mainly from their identification from the electromyographic (EMG) signal generated by the muscles using techniques as the Non-Negative Matrix Factorization (NMF) [1, 2].

However, the neural origin of synergies has been often debated [3]. Therefore, the authors of [4] proposed a paradigm to directly test whether the CNS recruits muscle synergies. In that work, subjects performed a virtual reaching task with a cursor either controlled by the isometric task generated at the hand or by EMG activity. In EMG control, the displacement of the cursor was computed in real-time as the product of an EMG-to-force mapping and the sample-by-sample EMG signal. The mapping could be then perturbed to simulate a virtual rearrangement of the forces generated by the muscles (virtual surgery). Participants practiced, during a sin-

gle experimental session, two different perturbations: a perturbation compatible with the muscle synergies (i.e. such that the participant could move the cursor in all directions with the previously extracted synergies) and one incompatible (i.e. such that the participant was required to recruit new muscle patters to make the cursor to span the whole workspace). If synergies were not organized by the CNS, but were only a description of the regularities of the motor commands generated by a different control strategy, there should not be any difference in the difficulty to adapt to the two types of perturbations. In contrast, participants adapted more easily to compatible perturbations. A significative difference was identified between the two perturbations in term of number of trials in which the participant successfully moved the cursor inside the target. These observations are in line with many studies [5] demonstrating that learning new motor skills requires more time than adapting known motor skills to a novel task. In fact, a modular controller can overcome in an easier way a perturbation that does not require learning of new synergies. A similar approach was proposed using a Brain Computer Interface (BCI) paradigm, in which monkeys moved a virtual cursor with their neural activity. Researchers demonstrated that, during a single experimental session, monkeys were not able to learn how to move the cursor if a perturbation that requires novel neural activity patterns, equivalent to the incompatible perturbations described by Berger and collaborators at the muscle level, is applied [6]. However,